ARTICLE

Check for updates

Coherent control of acoustic phonons in a silica fiber using a multi-GHz optical frequency comb

Mamoru Endo [1✉], Shota Kimura[1], Shuntaro Tani [1] & Yohei Kobayashi [1✉]

Multi-gigahertz mechanical vibrations that stem from interactions between light fields and matter—known as acoustic phonons—have long been a subject of research. In recent years, specially designed functional devices have been developed to enhance the strength of the light-matter interactions because excitation of acoustic phonons using a continuous-wave laser alone is insufficient. However, the strength of the interaction cannot be controlled appropriately or instantly using these structurally-dependent enhancements. Here we show a technique to control the effective interaction strength that does not operate via the material structure in the spatial domain; instead, the method operates through the structure of the light in the time domain. The effective excitation and coherent control of acoustic phonons in a single-mode fiber using an optical frequency comb that is performed by tailoring the optical pulse train. This work represents an important step towards comb-matter interactions.

[1] The Institute for Solid State Physics, The University of Tokyo, Chiba, Japan. ✉email: endo@ap.t.u-tokyo.ac.jp; yohei@issp.u-tokyo.ac.jp

Research on the interactions between light fields and acoustic phonons in lattice media has seen major advances over the past decade. This research holds enormous potential for both scientific studies and practical areas, where possible applications include the generation of ultra-low noise laser beams[1], optical frequency combs (OFCs)[2,3], coherent control[4–8], optical storage[9–11], slow and fast light generation[12], optical switching[13], and Brillouin cooling[14]. These light-matter interactions are caused by the permittivity changes in a medium caused by application of an incident electric field. Because of the weak nature of these interactions, specially designed photonic crystal fibers (PCFs)[2,5,15,16], suspended waveguides[17,18], and microresonators[1,9] have been devised to constrain both the optical fields and the acoustic modes and thus improve the interaction strength. However, with such structurally dependent enhancement of the interactions, there is an associated lack of the ability to control the interaction strength either dynamically or rapidly. In optical fibers, Brillouin scattering is the main process involved in the generation of acoustic phonons and this process requires long interaction lengths, such as those enabled by the use of continuous-wave (CW) or long pulsed (at least a few nanoseconds)[19] lasers. Long pulses, however, are unsuitable for use in telecommunication applications, which require fast and efficient control of the light-matter interactions.

We demonstrate here that if a second pulse is launched after a first pulse while remaining within the lifetime of a given acoustic phonon, this acoustic phonon can then be coherently enhanced or damped. To achieve this, we used picosecond pulses from our in-house developed multi-GHz OFC, which has its repetition frequency set to match the phonon resonance frequency (up to 16 GHz)[20]. Enhancement and damping can be controlled using either the pulse repetition frequency or the time delay between the pulses, which makes the multi-GHz OFC suitable for effective and coherent excitation. Coherent control of the acoustic phonon in the optical fiber can be performed using two CW lasers with their optical frequency difference matched to the phonon resonance frequency, which is a commonly used technique in the Brillouin optical time domain reflectometry[21,22] field and has been applied in several other fields[23,24]. Additionally, several researchers have demonstrated coherent control of a variety of targets with OFCs, including acoustic phonons[25], optical phonons[26,27], plasmons[28], and magnons[29]. In our method, we used multiple phase-locked comb teeth, i.e., ultra-stable pulsed light. Through manipulation of these pulse wave packets, coherent control has been demonstrated, regardless of the material properties, and specially designed materials are thus not required, indicating that our method is as versatile as other implemented ones[2,6,8,21]. To demonstrate this versatility, a commercial single-mode fiber was used to excite acoustic phonons from the silica by itself, without any aid from unique materials or structures (e.g., PCFs, waveguides, or microresonators). The proposed method will undoubtedly demonstrate its true value when combined with media composed of the special materials and structures that have been used in previous studies. Note that the control of acoustic phonons by the OFC described here is based on the structural tailoring of light in the optical frequency domain and the time domain. This goes back to the pioneering works in the early stage of nonlinear effect in optical fibers[30,31]. Our study can be described as a more flexible control of acoustic phonons by using a multi-GHz OFC that has been developed very recently.

Results and discussion

Photon–phonon interaction. Brillouin scattering results from the photon–phonon interactions that occur through the electrostriction effect[32]. When an acoustic phonon satisfies the phase-matching condition, it scatters light in the counter-propagating backward direction (BWD). This is illustrated in Fig. 1a, in which a CW (or long pulsed) laser beam propagates in the forward direction (FWD) with an angular frequency of ω_{FWD} (FWD optical, red line) and is then coupled into an optical fiber; the beam is scattered by thermally excited acoustic phonons in the fiber and a backscattered component at the down-shifted Stokes frequency, denoted by ω_{BWD} (BWD optical, purple line), is created. The density fluctuations caused by these two counter-propagating optical fields then create a traveling acoustic wave with an angular frequency of $\Delta\omega = \omega_{FWD} - \omega_{BWD}$ and a speed of $\frac{c\Delta\omega}{n_{FUT}\omega_{FWD}}$, where n_{FUT} is the refractive index of the fiber-under-test (FUT). Note here that in this situation, we focus solely on the phase velocities because the speeds of the light and acoustic waves are significantly different and the pump bandwidth is only several tens of GHz. This acoustic wave (FWD acoustic, sky blue line) then scatters the FWD optical beam to create BWD scattered light again and the cycle thus continues in this manner. When the speed of the FWD acoustic wave matches the speed of sound in the fiber (v_A), stimulated scattering occurs. The phase-matching condition is expressed as:

$$\omega_{AP} = \Delta\omega = 2\pi \times \frac{2n_{FUT}v_A}{\lambda_{FWD}} = \frac{2n_{FUT}v_A}{c}\omega_{FWD}, \quad (1)$$

where ω_{AP}, c, λ_{FWD} and n_{FUT} represent the angular frequency of the acoustic phonon (AP), the speed of light, the wavelength of the input FWD optical wave, and the refractive index of the FUT, respectively. The concept is illustrated in the dispersion diagram of Fig. 1b. In other words, the acoustic wave leads to a Brillouin gain and a Brillouin loss[12,33] at the Stokes and anti-Stokes frequencies of $\omega_{FWD} - \omega_{AP}$ and $\omega_{FWD} + \omega_{AP}$, respectively, as indicated by the gain and loss profiles shown in Fig. 1c. The BWD light has a broad spectrum because of the Doppler frequency shifts caused by the thermally excited acoustic phonons. The main scattering component at ω_{FWD} is referred to as Rayleigh scattering and the components that surround this main central peak are caused by the thermally excited acoustic phonons (we refer to these components as wings). Note that in Fig. 1c, the wings are not shown in scale. The Brillouin gain amplifies the minuscule Stokes component contained in the wing at $\omega_{FWD} - \omega_{AP}$. Under these conditions, the photon–phonon interaction strength is weak and either long interaction lengths or specially designed structures are needed to enhance this strength. The typical frequency for acoustic phonons in a silica fiber is ~16 GHz for pump light at a wavelength of 1 μm and the phonons have a linewidth δ of several tens of MHz.

Figure 1d–f are equivalent to Fig. 1a–c, respectively, only they relate to the case in which the pump beam is a train of pulses, such as that of an OFC with a repetition frequency of $\omega_{rep}/(2\pi)$. The number of comb teeth is N and the optical angular frequency of the nth comb tooth is $\omega_{FWD}^{(n)} = \omega_{FWD}^{(1)} + (n-1)\omega_{rep}$. Figure 1d–f depict the instances when the repetition frequency is equal to the phonon resonance frequency, i.e., where $\omega_{rep} = \omega_{AP}$. The gratings formed by the acoustic phonons reflect the FWD light wave along the optical fiber. For example, as shown in Fig. 1d, the reflected FWD light waves at points A and B interfere constructively and the amplitude of the BWD light wave is enhanced when $\omega_{rep} = \omega_{AP}$. In contrast, when $\omega_{rep} \neq \omega_{AP}$, the reflected FWD light waves at both points are averaged out and no enhancement can be observed. More specifically, this causes the backscattered component at the Stokes (anti-Stokes) angular frequency of the first comb tooth, given by $\omega_{FWD}^{(1)} - \omega_{AP}$, ($\omega_{FWD}^{(1)} + \omega_{AP}$), to have a gain (loss) spectrum similar to that depicted in Fig. 1c. However, as
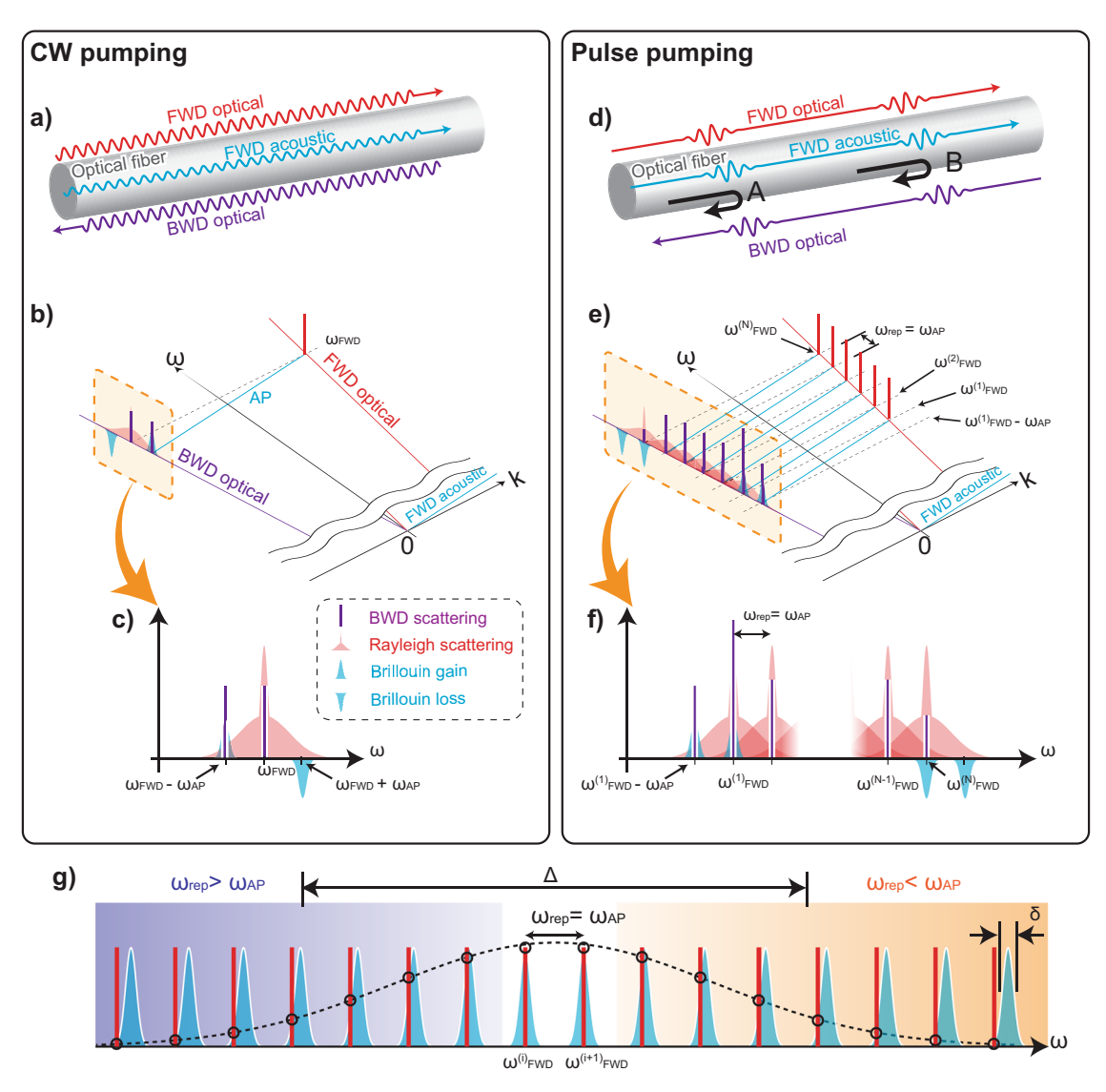
Fig. 1 Conceptual images of Brillouin scattering in a fiber and dispersion diagrams (not to scale) of the light and acoustic waves. In the continuous-wave (CW) pumping case: **a**–**c** show the in-fiber illustration, the dispersion diagram, and the backward (BWD) optical spectrum, respectively. In the pulsed (multi-mode) pumping case: **d**–**f** show the in-fiber illustration, the dispersion diagram, and the BWD optical spectrum, respectively. Red lines: forward (FWD) optical waves or comb teeth; purple lines: BWD optical waves or comb teeth; sky blue lines: FWD acoustic waves or longitudinal modes. In **b**, **c**, **e**, **f**, the areas indicated in red are the Rayleigh scattering components with wings and the areas in sky blue denote the Brillouin gain(s) and loss(es) due to the FWD acoustic waves. **g** Relaxed phase-matching condition. The repetition frequency ω_{rep} is kept constant, while ω_{AP}, represented by the blue Brillouin lines, is sliding with respect to ω_{FWD} due to phase mismatch. The dashed black line with the width of Δ represents the effective Brillouin gain as a function of the optical angular frequency.

shown in Fig. 1f, the potential of this technique is demonstrated in the gain spectrum of the other comb tooth with the frequency of $\omega_{FWD}^{(2)} = \omega_{FWD}^{(1)} + \omega_{AP}$. The Brillouin gain due to the next comb tooth at $\omega_{FWD}^{(2)}$ is added to the center of the Rayleigh scattering of the comb tooth at $\omega_{FWD}^{(1)}$, where the amplitude is much higher than that at the wings, and a markedly enhanced BWD component is thus produced. At the frequencies of all the other comb teeth, the Brillouin losses and gains almost cancel each other out and this tendency passes through to the anti-Stokes frequencies of the two highest comb teeth of the OFC; for the first of the two comb teeth, the Brillouin loss attenuates the center of the Rayleigh scattering of the last comb tooth at $\omega_{FWD}^{(N)}$, while in the case of the second comb tooth, the scenario matches that depicted at the anti-Stokes frequency in Fig. 1c. In the Methods section, we provide more

detailed description of the imperfection of the gain and loss balancing.

It should be noted here that the phonon frequency is dependent on the optical frequency of the pump light, as indicated by Eq. (1), and the centers of the backscattered Rayleigh, Stokes, and anti-Stokes gains are not matched perfectly over all the comb teeth of the OFC, as illustrated in Fig. 1g. The red lines in the figure represent the comb teeth and the blue areas represent the Brillouin gain profiles. The profile of the Brillouin gain in a conventional single-mode fiber at room temperature typically has a spectral width of several tens of MHz and the phase-matching conditions are more relaxed for pump light with spectral widths in the sub-hundred GHz range (corresponding to pulse durations of several tens of ps). This is discussed in detail in the Methods section.
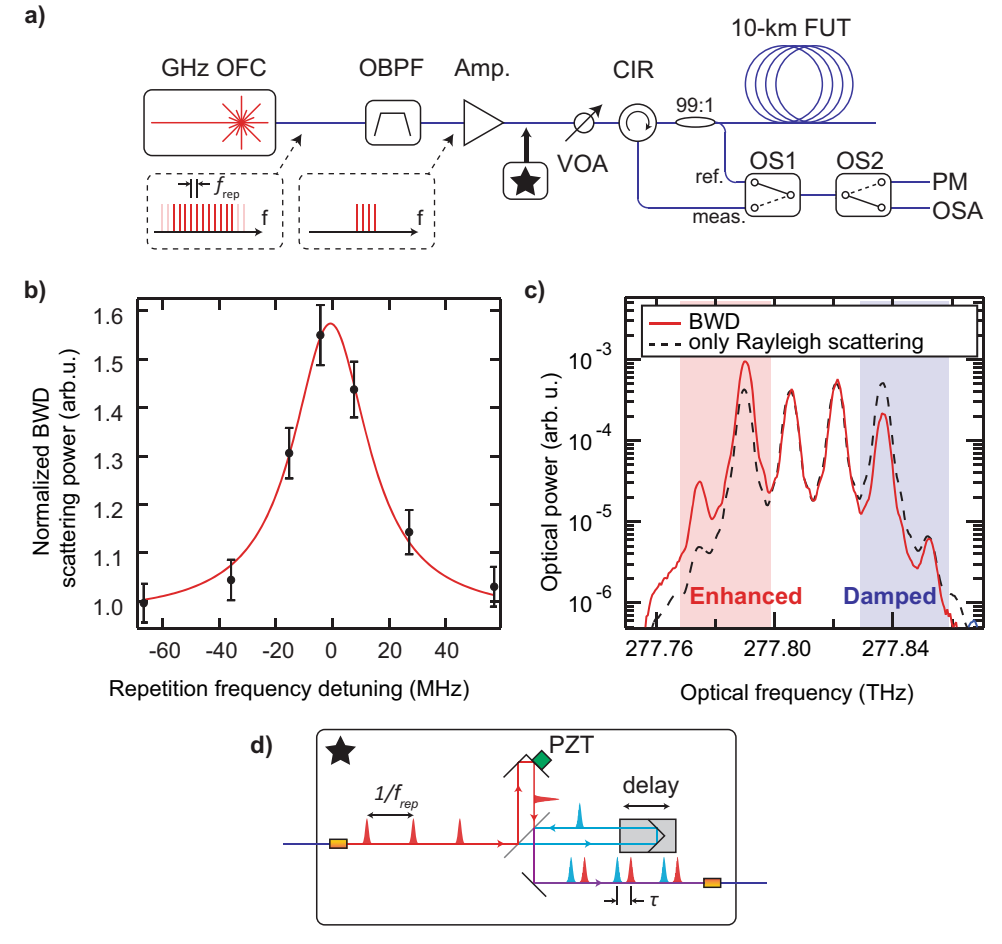
Fig. 2 Experimental apparatus and results. **a** Experimental apparatus. GHz OFC: optical frequency comb based on a Yb:Y_2O_3 ceramic Kerr-lens mode-locked laser with repetition rates of 7.8 or 15.6 GHz. OBPF: optical band-pass filter based on a grating spectrometer with resolution of 2 GHz. Amp.: Three-stage optical amplifier (composed of one semiconductor optical amplifier and two ytterbium-doped fiber amplifiers). VOA: variable optical attenuator. CIR: optical circulator. OS: optical switch. FUT: fiber-under-test. OSA: optical spectrum analyzer with resolution of 4 GHz. PM: optical power meter. The black star: the part to be added in the next experiment (see (**d**)). **b** BWD power (corresponding to the phonon amplitude) as a function of the repetition rate detuning, measured using an input power of 20 mW. The red trace shows the Lorentzian fitting of the black experimental data points. The error bars represent one standard deviation from the mean value. **c** BWD spectra at the repetition rate of 15.57 GHz. Black dashed line: Rayleigh scattering used as the reference; red solid line: BWD spectrum. The red and blue shaded areas correspond to the Brillouin gain and loss in Fig. 1f, respectively. **d** Michelson interferometer used in the double pulse experiment at the black star in **a**. PZT: piezo-actuator used for scanning of the arm's length.

Repetition frequency dependence of the acoustic phonons in a silica fiber. Figure 2a shows a schematic illustration of the experimental apparatus; further details can be found in the Methods section. To observe the relationship between the repetition rate of the OFC and the acoustic phonons, we used an OFC with a repetition rate of 15.6 GHz and a pulse duration of 152 fs. The OFC output was filtered using an optical band-pass filter (OBPF) to select four of the comb teeth, i.e., the optical bandwidth was $4 \times 15.6\,\mathrm{GHz} = 62.4\,\mathrm{GHz}$ (see the Methods). The output power was then amplified using three-stage optical amplifiers to produce a 20 ps pulse train with a maximum average power of 100 mW. The signal-to-noise ratio of the input spectrum was more than 40 dB and the background noise (e.g., the amplified spontaneous emissions of the optical amplifiers) could be ignored. The optical pulses were coupled into a 10-km-long FUT with a core diameter of 11 µm (FutureGuide-SR15E, Fujikura Ltd., Tokyo, Japan) after passing through an optical circulator (CIR). The input and the BWD scattered light waves were measured using an optical spectrum analyzer (OSA) and a power meter (PM) through a 99:1 fiber coupler and two optical switches (OS1 and OS2). The input is used as the reference beam (ref.) and the BWD scattering light corresponds to the phonon amplitude

(meas.), as described in the Methods section. Figure 2b represents the power of the BWD light as a function of the detuning of the OFC repetition frequency for an input power of 20 mW, where a detuning of 0 MHz corresponds to the phonon resonance frequency of 15.57 GHz. The OFC's repetition frequency is tuned using a linear stage and a piezoelectric actuator for coarse and fine tuning of the OFC cavity, respectively (see the Methods). The black dots and the error bars represent the measured values and the red solid line shows the Lorentzian fit of the results. The power of the BWD light is normalized with respect to the estimated Rayleigh scattering power (see the Methods). The BWD power was enhanced by the factor of 1.6 when the repetition frequency detuning was zero, i.e., when the repetition frequency matched the phonon resonance (15.57 GHz) within the phonon linewidth ($\sim\delta = 21$ MHz in our case). This efficient excitation was made possible by using a continuous train of pulses with a repetition frequency that was close to the target phonon resonance frequency, in contrast to the detuned pulse train. As shown in Fig. 2c, where the red line represents the spectrum of the BWD optical wave and the black dotted line represents the Rayleigh scattering alone, which serves as a reference, the Stokes component (area in red) was enhanced and the energies of the higher

frequency components were transferred to this component. This experiment serves to verify that acoustic phonons can be excited using OFCs with repetition rates that are equal to the phonon resonance. Note that in Fig. 2c, each comb tooth has a linewidth of ~4 GHz; this is caused by the limited frequency resolution of the OSA. The actual OFC linewidth after OBPF is suitably narrower than the phonon linewidth[20]. Also, it is known that during Brillouin scattering process, the linewidth of the input OFC is not greatly affected[34]. Therefore, we conclude that the linewidth in Fig. 2c is sufficiently narrower than 4 GHz.

Coherent control of the acoustic photons. To demonstrate coherent control of the acoustic phonons, the repetition frequency of the OFC was changed to 7.8 GHz (i.e., half of the phonon resonance frequency) by realigning the laser cavity and the bandwidth of the OBPF was also changed to select four comb teeth, such that the optical bandwidth was 4×7.8 GHz = 31.2 GHz. A Michelson interferometer (MI) was then inserted between Amp. and VOA (indicated by the black star in Fig. 2a) to produce double pulses, as shown in Fig. 2d (see the Methods for further details). Here, the pulse delay was normalized with respect to the phonon oscillation period, i.e., $\tau = 1$ corresponds to 64 ps. As depicted in Fig. 3a, the phonon amplitude can be accumulated when the interval used for a series of optical pulses matches an integer multiple of the phonon oscillation cycle (i.e., $\tau = m$, where m is an integer), which is identical to the results from the previous experiment illustrated in Fig. 2. In contrast, when $\tau = \frac{1}{2} + m$, while the first pulse does excite the phonon, the second pulse then damps it (Fig. 3b shows the case where $\tau = 0.5$). As a result, the phonon's amplitude is suppressed, even when the fundamental repetition frequency of the OFC is matched to the half of the phonon resonance frequency.

In the experiments, by sweeping the length of one of the interferometer's arms using a motorized stage, double pulses with normalized time delays ranging from 0 to 1.5 of the inverse of the phonon resonance frequency could be obtained. Figure 3d shows the phonon amplitude as a function of this normalized delay. The red trace represents the on-resonance case (where $\omega_{rep} = \omega_{AP}/2$) and the blue trace represents the out-of-resonance case (where $\omega_{rep} = \frac{\omega_{AP}}{2} + 2\pi \times 34$ MHz). The red trace shows a strong dependence on the time interval of the double pulse. When the normalized interval was set to 0, 1, or 2, the phonon amplitude increased. In contrast, the phonon amplitude was suppressed when the delay was set at 0.5 and 1.5. The enhancement factor is ~1.8 and the enhancement factors at $\tau = 1$ and $\tau = 0$, 2 are almost the same. This is because the phonon's relaxation time of 50 ns (i.e., the inverse of $\delta = 20$ MHz) is much longer than the pulse interval of 128 ps. Because the fundamental repetition frequency is decreased from 15.6 to 7.8 GHz, the optical spectra shown in Fig. 1f is changed as shown in Fig. 3c. The dashed line in Fig. 3d shows the simulated results, which showed good agreement with the experimental results. Note that in the simulation, we used the estimated Rayleigh scattering spectrum based on the actual incident light spectrum, which can be subject to fluctuations due to instability or interference effects in the experimental apparatus. In particular, the OBPF with its very narrow bandwidth is highly sensitive to turbulence. Because of these fluctuations, the simulation results are skewed. Figure 3e, f show the optical spectra of the BWD light as functions of the normalized pulse interval (where (e) is at resonance and (f) is out of resonance). The Stokes components in Fig. 3e are enhanced when the normalized pulse interval is 0, 1, or 2, which supports the concept illustrated in Fig. 3a–c. In contrast, when the phonon is out of resonance, the optical spectrum does not change, even when the pulse interval changes (Fig. 3f). Note that, in Fig. 3e, the Stokes

components (around the optical frequencies of 278.015 and 278.024 THz) are shown to be stronger at $\tau = 0$ and 2 than at $\tau = 1$. This is due to the nonlinear effect (four-wave mixing between the comb tooth) that develops at $\tau = 0$ or 2, because the energy per single pulse is stronger than that at $\tau = 1$.

Conclusion

In conclusion, we have demonstrated coherent control of acoustic phonons in a standard single-mode fiber using a repetition-frequency-tailored multi-GHz OFC. The phonon amplitude was coherently enhanced using this method and the acoustic phonon was also controlled using the optical pulse delay. Although the enhancement factors in this proof-of-principle experiment are not as significant as those obtained when using special materials such as PCFs, our approach to the control of the effective interaction strength between photons and phonons can be applied in various areas of science, and in the field of telecommunications in particular. For example, as shown by Wiederhecker et al.[6], a series of pulses in a train (27 pulses here) can excite optical phonons significantly in a PCF. Our scheme can easily be combined with the setup used in such experiments and highly efficient dynamic control can then be realized. This technique can utilize a myriad of coherent pulses. In other words, we can ultimately achieve coherent control using the number of pulses (~160,000 pulses), which is the repetition frequency of the OFC (~16 GHz) divided by the linewidth of the OFC (~100 kHz, see Method). In this work, we focus on the acoustic phonon experiments as a proof-of-principle, but the result opens the way toward an optical scheme to enable manipulation of (quasi) particles in the field of solid-state physics, in which there are numerous intriguing elemental excitations, including optically accessible skyrmions[35] and magnons[36,37]. The proposed technique could be extended to the control of multiple types of excitations simultaneously by combining it with the other degrees of freedom of the OFC, e.g., the carrier-envelope offset frequency, the pulse duration or the chirp. We believe that the application of OFCs to study and manipulate particles has major potential for use in the solid-state physics field and that our work represents an important step in the research into comb-matter interactions.

Methods

Light source (spectrally filtered multi-GHz OFC). An OFC based on a Kerr-lens mode-locked Yb:Y$_2$O$_3$ ceramic laser with a repetition rate of 7.8 or 15.6 GHz was used. The center wavelength and the pulse duration of this OFC were 1080 nm (278 THz) and 152 fs, respectively. The typical spectrum width is 12 nm (3.08 THz). When the repetition frequency was changed from 15.6 to 7.8 GHz or vice versa, we also realigned the laser cavity. Coarse tuning of the repetition frequency was performed using a linear stage and the repetition frequency could be tuned over several hundred MHz using this method. For fine tuning, the repetition frequency was stabilized with reference to an analog signal generator via a phase-locked loop circuit and a piezoelectric actuator that was mounted on one of the cavity mirrors. The repetition frequency stability was better than 10^{-12} at 1 s, which is more than sufficient for our experimental demonstration. Other details of this OFC can be found in the literature[20]. The free-running fluctuations of the carrier-envelope offset and the optical frequencies were negligible, and we did not apply any stabilization to these fluctuations during the experiments. The OFC's linewidth is estimated to be 100 kHz approximately by measuring the heterodyne signal between one of the comb teeth and a narrow linewidth CW laser.

The OFC output was spectrally filtered using a hand-made OBPF with maximum frequency resolution of 2 GHz at a wavelength of 1080 nm. This filter was based on a multi-pass, high-resolution spectrograph[38] and would let four comb teeth through, as illustrated in Fig. 2c. The filtered output was amplified using a three-stage optical amplifier (a cascade composed of one semiconductor optical amplifier followed by two Yb-doped fiber amplifiers) up to a maximum average power of more than 100 mW. The output power could be tuned using a variable optical attenuator that was assembled in-house. The input power calibration was performed by measuring the optical power through the 99:1 coupler and the PM shown in Fig. 2a. Although the small peaks on both sides of the four main lines shown in Fig. 2c were caused by the imperfections of the OBPF, the contributions of these peaks are 20 dB smaller than those of the main peaks and can thus be ignored when the total BWD power is considered. The anti-Stokes small peaks
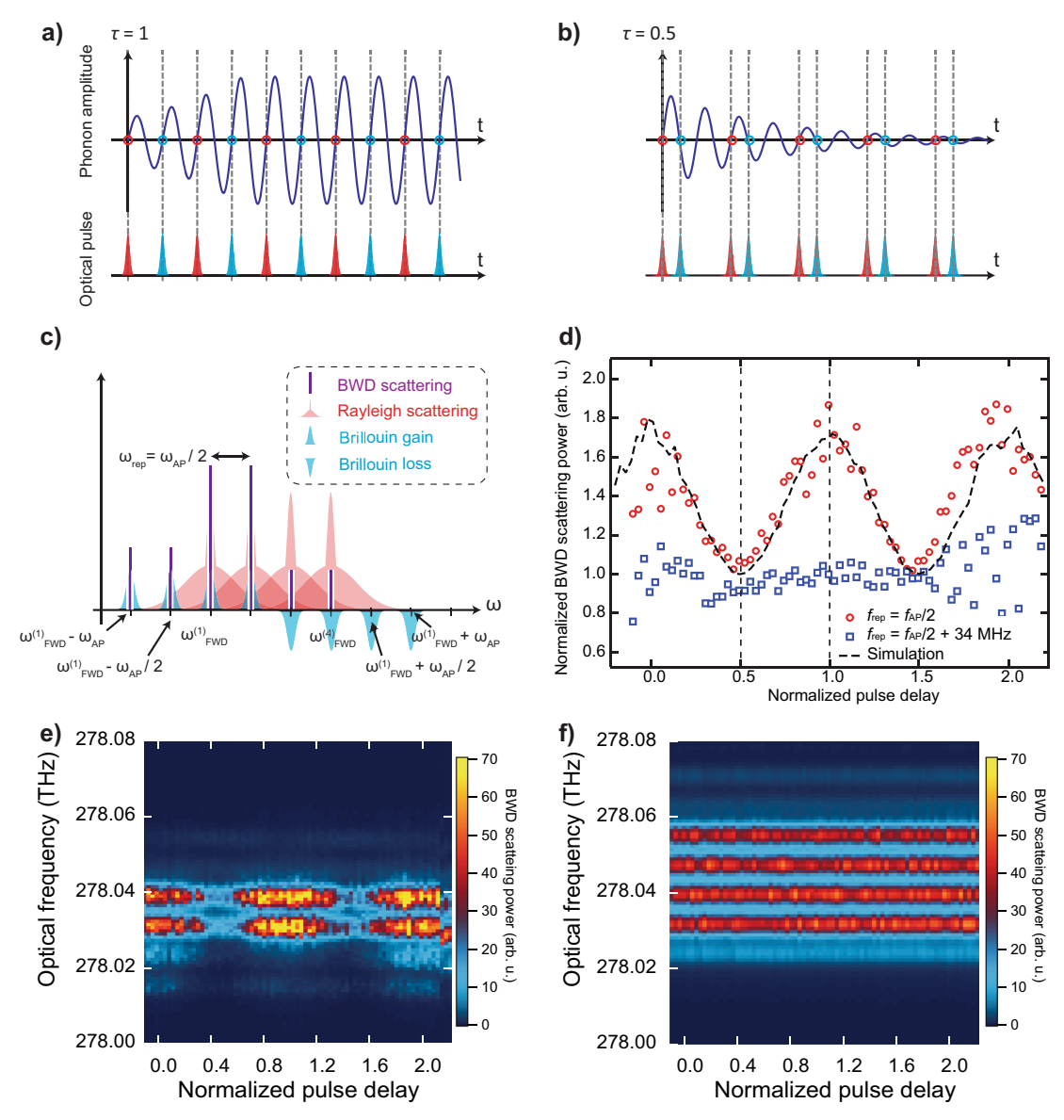
Fig. 3 Conceptual images and results of coherent control of the phonons using double pulses. Time domain pictures for **a** $\tau = 1$ and **b** 0.5 delays, respectively. The pulse delay was normalized with respect to the phonon oscillation period. **a** Growth of the phonon amplitude along the optical pulse train. In contrast, **b** shows the phonon amplitude, which is excited by the red pulses and damped by the blue pulses. **c** BWD spectrum when $\tau = 1$. **d** BWD powers (corresponding to the phonon amplitudes) as a function of the normalized pulse delay τ. Red-circles and blue-square markers represent the experimental data with the repetition angular frequencies of $\omega_{AP}/2$ and $\frac{\omega_{AP}}{2} + 2\pi \times 34$ MHz, respectively. The dashed line represents the simulation results. **e, f** Show the optical spectra of the BWD light waves at resonance and when out of resonance, respectively.

(around the frequency of 277.85 THz) were not damped. This is because the passband of the OBPF was shifted slightly during the experiments because of thermal drift or mechanical vibrations. However, the contribution of these peaks can also be ignored.

Preparation of the double pulse. A Michelson interferometer (MI) was used to generate the double pulses, as shown in Fig. 2d. In one of the interferometer's arms, a stepper-motorized mechanical stage was used to tune the pulse time interval between 0 and 160 ps. A piezo-actuator and a noise source were used to scan the arm length to average out the spectral interference of the double pulse to achieve a higher signal-to-noise ratio. Without this piezo-actuator, sub-wavelength stabilization of the interferometer arm would be required, at the cost of lengthy scan times and data averaging. While the use of the piezo-actuator reduced the time resolution of the experiment to several hundreds of femtoseconds, this very high time resolution was not actually required for our measurements. The peak-to-peak amplitude and the bandwidth were measured to be 3 μm and 300 Hz, respectively.

Estimation of Rayleigh scattering. Estimation of the Rayleigh scattering spectra used to normalize the BWD scattering spectra was performed using a weak CW

laser. We injected the weak CW laser beam with a wavelength of 1080 nm and an average power of 10 μW, which is significantly smaller than the stimulated Brillouin scattering threshold of 15 mW for our 10-km-long FUT, into the system through the circulator. The input and BWD scattering powers were measured using the PM by appropriate setting of OS1 (meas. and ref. positions, respectively). The resulting ratio was then used to calculate the Rayleigh scattering spectrum by multiplying the ratio by the input spectrum, which was monitored constantly by the OSA to act as the reference spectrum.

Photon–phonon interaction and phonon amplitude estimation from the BWD spectrum. The field distributions of the FWD and BWD optical modes in the fiber are expressed as follows:

$$E_{\mathrm{FWD}}(z, t) = \sum_n A_{\mathrm{FWD}}^{(n)}(z, t) \exp\left[\mathrm{i}\left(k_{\mathrm{FWD}}^{(n)} z - \omega_{\mathrm{FWD}}^{(n)} t\right)\right] + \mathrm{c.c.}$$

$$E_{\mathrm{BWD}}(z, t) = \sum_n A_{\mathrm{BWD}}^{(n)}(z, t) \exp\left[\mathrm{i}\left(-k_{\mathrm{BWD}}^{(n)} z - \omega_{\mathrm{BWD}}^{(n)} t\right)\right] + \mathrm{c.c.}$$

where $A_{\mathrm{FWD}}^{(n)}(z,t)$ and $A_{\mathrm{BWD}}^{(n)}(z,t)$ are the amplitudes; $k_{\mathrm{FWD}}^{(n)} = \frac{n_{\mathrm{FUT}}\omega_{\mathrm{FWD}}^{(n)}}{c}$, $k_{\mathrm{BWD}}^{(n)} = \frac{n_{\mathrm{FUT}}\omega_{\mathrm{BWD}}^{(n)}}{c}$ are the wave numbers; and c.c. represents the complex conjugate.

The intensities of the two fields are defined as

$$I_{\mathrm{FWD}}^{(n)} := 2n_{\mathrm{FUT}}\epsilon_0 c A_{\mathrm{FWD}}^{(n)}(z,t)\left(A_{\mathrm{FWD}}^{(n)}(z,t)\right)^*$$

$$I_{\mathrm{BWD}}^{(n)} := 2n_{\mathrm{FUT}}\epsilon_0 c A_{\mathrm{BWD}}^{(n)}(z,t)\left(A_{\mathrm{BWD}}^{(n)}(z,t)\right)^*.$$

The following coupling differential equations were then obtained to describe the photon–phonon interactions.

$$\frac{dI_{\mathrm{FWD}}^{(n)}}{dz} = gI_{\mathrm{FWD}}^{(n)}I_{\mathrm{BWD}}^{(n+1)} - gI_{\mathrm{FWD}}^{(n)}I_{\mathrm{BWD}}^{(n-1)} - \alpha I_{\mathrm{FWD}}^{(n)}$$

$$-\frac{dI_{\mathrm{BWD}}^{(n)}}{dz} = gI_{\mathrm{BWD}}^{(n)}I_{\mathrm{FWD}}^{(n+1)} - gI_{\mathrm{BWD}}^{(n)}I_{\mathrm{FWD}}^{(n-1)} - \alpha I_{\mathrm{BWD}}^{(n)}$$

$$\rho(z,t) = \epsilon_0 \gamma_e q^2 \sum_n \frac{A_{\mathrm{FWD}}^{(n)}\left(A_{\mathrm{BWD}}^{(n+1)}\right)^*}{\Omega_{\mathrm{B}}^2 - \omega_{\mathrm{rep}}^2 - i\omega_{\mathrm{rep}}\Gamma_{\mathrm{B}}},$$

where g is the Brillouin linear gain; $\rho(z,t)$ is the intensity of the FWD acoustic wave; γ_e is the electrostrictive constant; $q \sim 2k_{\mathrm{FWD}}^{(1)}$ is the wavenumber of the FWD acoustic wave; Γ_{B} is the Brillouin linewidth; and Ω_{B} is the Brillouin frequency shift. In the steady state, the intensity of the acoustic phonon $\rho(z,t)$ can be estimated using $A_{\mathrm{FWD}}^{(n)}$ and $A_{\mathrm{BWD}}^{(n)}$. The Brillouin gain g is dependent on the optical frequency and we assume here that g is a Lorentz type function, as shown in Fig. 1g. Specifically, $g(\omega) = g_0 \frac{(\delta/2)^2}{(\omega-\omega_0)^2 + (\delta/2)^2}$, where ω_0 is the center optical angular frequency, g_0 is the peak Brillouin gain, and δ is the linewidth of the acoustic phonon. If the strict phase-matching condition is satisfied at the optical frequency $\omega_{\mathrm{FWD}}^{(i)}$, then the repetition frequency must be $\omega_{\mathrm{rep}} = \omega_{\mathrm{AP}}(\omega_{\mathrm{FWD}}^{(i)})$. In contrast, at the higher or lower comb teeth, the Brillouin gain is reduced, as shown in Fig. 1g. The relaxed phase-matching bandwidth Δ (illustrated by the black dashed line with the width of Δ in Fig. 1g) can be calculated using $\Delta \sim \delta \times \omega_{\mathrm{FWD}}/\omega_{\mathrm{rep}}$. Under our experimental conditions, the bandwidth was ~360 GHz. This means that even if a broad pump source such as a femtosecond laser is used, only ten comb teeth contribute to the phonon excitation. In the first and second experiments, the bandwidths of the pump OFC were 62.4 and 31.2 GHz, respectively. This was because we used only four comb teeth in these experiments.

From the equations above, the intensity of the FWD acoustic phonon can be estimated based on the amplitudes of the BWD and FWD light fields. In the experiments, we assumed that the FWD light fields were constant. To calculate the simulated dashed line shown in Fig. 3c, we solved these differential equations in MATLAB and in the manner described in the supplemental information of reference[15].

Imbalance of the gain and loss. In Fig. 1f and in the main text, we assume that the values of the gain and loss among the intermediate comb teeth are almost balanced. However, strictly speaking, a slight imbalance remains. We describe this imbalance effect quantitatively here.

Perfect phase-matching conditions are assumed to occur when the frequency of $\omega_0 = (\omega_{\mathrm{FWD}}^{(i)} + \omega_{\mathrm{FWD}}^{(i+1)})/2$, where $i > 1$. Specifically, the phonon frequency and the repetition frequency can be related using the following equation:

$$\omega_{\mathrm{AP}} = \omega_{\mathrm{rep}} = \frac{2n_{\mathrm{FUT}}\nu_A}{c}\omega_0.$$

Now let us consider the gain and loss profiles for comb tooth j. The gain for mode j is caused by the higher adjacent mode $J + 1$. The angular frequency of the gain peak is calculated using

$$\omega^{(j+1)} - \frac{2n_{\mathrm{FUT}}\nu_A}{c}\omega^{(j+1)}.$$

Then, the frequency difference between the gain peak and the comb tooth is given by:

$$\omega^{(j+1)} - \frac{2n_{\mathrm{FUT}}\nu_A}{c}\omega^{(j+1)} - \omega^{(j)} = \omega_{\mathrm{rep}}\left(1 - \frac{\omega^{(j+1)}}{\omega_0}\right) = \frac{\omega_{\mathrm{rep}}^2}{\omega_0}\left(i - j - \frac{1}{2}\right).$$

In the same manner, the frequency difference between the loss peak and the comb tooth is given by:

$$\frac{\omega_{\mathrm{rep}}^2}{\omega_0}\left(-i + j - \frac{3}{2}\right).$$

The imbalance is then calculated using

$$g\left(\omega^{(j)} + \frac{\omega_{\mathrm{rep}}^2}{\omega_0}\left(i - j - \frac{1}{2}\right)\right) - g\left(\omega^{(j)} + \frac{\omega_{\mathrm{rep}}^2}{\omega_0}\left(-i + j + \frac{3}{2}\right)\right).$$

Note that we assume that the gain and loss have the same profile (i.e., the same Lorentzian profiles with the same width δ), and that the comb teeth have the same

mode powers. In a worst-case estimation, the imbalance between the gain and the loss is calculated to be ~0.9%, which can be regarded as negligible for our experiment.

Measurement of the acoustic phonon resonance frequency. The acoustic phonon resonance frequency was measured using the same apparatus used to estimate the Rayleigh scattering, as described earlier. We increased the input power to 20 mW, which is higher than the stimulated Brillouin scattering threshold of 15 mW, and a heterodyne beat frequency between the FWD and BWD light waves was measured using a high-speed InGaAs photodiode and an electrical spectrum analyzer.

Data availability

All data needed to evaluate the conclusions are present in the paper. Additional data related to this paper are available from the corresponding authors on reasonable request.

References

1. Liang, W. et al. High spectral purity Kerr frequency comb radio frequency photonic oscillator. *Nat. Commun.* **6**, 7957 (2015).
2. Pang, M. et al. Stable subpicosecond soliton fiber laser passively mode-locked by gigahertz acoustic resonance in photonic crystal fiber core. *Optica* **2**, 339 (2015).
3. Dong, M. & Winful, H. G. Unified approach to cascaded stimulated Brillouin scattering and frequency-comb generation. *Phys. Rev. A* **93**, 043851 (2016).
4. Merklein, M. et al. Enhancing and inhibiting stimulated Brillouin scattering in photonic integrated circuits. *Nat. Commun.* **6**, 6396 (2015).
5. Kang, M. S., Brenn, A. & Russell, P. St. J. All-optical control of gigahertz acoustic resonances by forward stimulated interpolarization scattering in a photonic crystal fiber. *Phys. Rev. Lett.* **105**, 153901 (2010).
6. Wiederhecker, G. S., Brenn, A., Fragnito, H. L. & Russell, P. S. J. Coherent control of ultrahigh-frequency acoustic resonances in photonic crystal fibers. *Phys. Rev. Lett.* **100**, 203903 (2008).
7. Koehler, J. R., Noskov, R. E., Sukhorukov, A. A., Novoa, D. & Russell, P. S. J. Coherent control of flexural vibrations in dual-nanoweb fibers using phase-modulated two-frequency light. *Phys. Rev. A* **96**, 063822 (2017).
8. Diamandi, H. H., London, Y., Bashan, G., Bergman, A. & Zadok, A. Highly-coherent stimulated phonon oscillations in a multi-core optical fiber. *Sci. Rep.* **8**, 9514 (2018).
9. Dong, C.-H. et al. Brillouin-scattering-induced transparency and non-reciprocal light storage. *Nat. Commun.* **6**, 6193 (2015).
10. Pang, M., He, W., Jiang, X. & Russell, P. S. J. All-optical bit storage in a fibre laser by optomechanically bound states of solitons. *Nat. Photonics* **10**, 454–458 (2016).
11. Merklein, M., Stiller, B., Vu, K., Madden, S. J. & Eggleton, B. J. A chip-integrated coherent photonic-phononic memory. *Nat. Commun.* **8**, 574 (2017).
12. Thévenaz, L. Slow and fast light in optical fibres. *Nat. Photonics* **2**, 474–481 (2008).
13. Kang, M. S., Butsch, A. & Russell, P. S. J. Reconfigurable light-driven opto-acoustic isolators in photonic crystal fibre. *Nat. Photonics* **5**, 549–553 (2011).
14. Bahl, G., Tomes, M., Marquardt, F. & Carmon, T. Observation of spontaneous Brillouin cooling. *Nat. Phys.* **8**, 203–207 (2012).
15. Kang, M. S., Nazarkin, A., Brenn, A. & Russell, P. S. J. Tightly trapped acoustic phonons in photonic crystal fibres as highly nonlinear artificial Raman oscillators. *Nat. Phys.* **5**, 276–280 (2009).
16. Dainese, P. et al. Stimulated Brillouin scattering from multi-GHz-guided acoustic phonons in nanostructured photonic crystal fibres. *Nat. Phys.* **2**, 388–392 (2006).
17. Shin, H. et al. Tailorable stimulated Brillouin scattering in nanoscale silicon waveguides. *Nat. Commun.* **4**, 1944 (2013).
18. Van Laer, R., Kuyken, B., Van Thourhout, D. & Baets, R. Interaction between light and highly confined hypersound in a silicon photonic nanowire. *Nat. Photonics* **9**, 199–203 (2015).
19. Faris, G. W., Jusinski, L. E. & Hickman, A. P. High-resolution stimulated Brillouin gain spectroscopy in glasses and crystals. *J. Opt. Soc. Am. B* **10**, 587 (1993).
20. Endo, M., Ito, I. & Kobayashi, Y. Direct 15-GHz mode-spacing optical frequency comb with a Kerr-lens mode-locked Yb:Y2O3 ceramic laser. *Opt. Express* **23**, 1276 (2015).
21. Thévenaz, L. Brillouin distributed time-domain sensing in optical fibers: state of the art and perspectives. *Front. Optoelectron. China* **3**, 13–21 (2010).

22. Beugnot, J.-C., Tur, M., Mafang, S. F. & Thévenaz, L. Distributed Brillouin sensing with sub-meter spatial resolution: modeling and processing. *Opt. Express* **19**, 7381 (2011).
23. Song, K. Y., Zou, W., He, Z. & Hotate, K. All-optical dynamic grating generation based on Brillouin scattering in polarization-maintaining fiber. *Opt. Lett.* **33**, 926 (2008).
24. Picholle, E., Montes, C., Leycuras, C., Legrand, O. & Botineau, J. Observation of dissipative superluminous solitons in a Brillouin fiber ring laser. *Phys. Rev. Lett.* **66**, 1454–1457 (1991).
25. Ip, M. et al. Phonon Lasing from Optical Frequency Comb Illumination of Trapped Ions. *Phys. Rev. Lett.* **121**, 43201 (2018).
26. Yu, M. et al. Raman lasing and soliton mode-locking in lithium niobate microresonators. *Light Sci. Appl.* **9** (2020).
27. Hase, M., Katsuragawa, M., Constantinescu, A. M. & Petek, H. Frequency comb generation at terahertz frequencies by coherent phonon excitation in silicon. *Nat. Photonics* **6**, 243–247 (2012).
28. Anh, N. D. et al. Plasmonic dynamics measured with frequency-comb-referenced phase spectroscopy. *Nat. Phys.* **15**, 132–137 (2019).
29. Braggio, C., Carugno, G., Guarise, M., Ortolan, A. & Ruoso, G. Optical manipulation of a magnon-photon hybrid system. *Phys. Rev. Lett.* **118**, 107205 (2017).
30. Cotter, D. Stimulated Brillouin scattering in monomode optical fibre. *J. Opt. Commun.* **4**, 10–19 (1983).
31. Cotter, D. Suppression of stimulated Brillouin scattering during transmission of high-power narrowband laser light in monomode fibre. *Electron. Lett.* **18**, 638–640 (1982).
32. Chiao, R. Y., Townes, C. H. & Stoicheff, B. P. Stimulated brillouin scattering and coherent generation of intense hypersonic waves. *Phys. Rev. Lett.* **12**, 592–595 (1964).
33. Li, H. et al. Frequency domain staring pump-probe technique for Brillouin gain/loss spectrum measurement. *Appl. Opt.* **56**, 5745 (2017).
34. Terra, O. A single mode from optical frequency comb with relative stability of 10−17 using stimulated brillouin scattering. *J. Light. Technol.* **37**, 5363–5369 (2019).
35. Ogawa, N., Seki, S. & Tokura, Y. Ultrafast optical excitation of magnetic skyrmions. *Sci. Rep.* **5**, 9552 (2015).
36. Chumak, A. V., Vasyuchka, V. I., Serga, A. A. & Hillebrands, B. Magnon spintronics. *Nat. Phys.* **11**, 453–461 (2015).
37. Vogel, M. et al. Optically reconfigurable magnetic materials. *Nat. Phys.* **11**, 487–491 (2015).
38. Endo, M., Sukegawa, T., Silva, A. & Kobayashi, Y. Subgigahertz-resolution table-top spectrograph calibrated with a 4-GHz optical frequency comb. *J. Astron. Telesc. Instrum. Syst.* **6**, 020501 (2020).

Author contributions
M.E. was responsible for the overall execution of the experiments. M.E. and S.K. developed the laser source. M.E. and S.T. developed analytical models to explain the measured data with the assistance of Y.K. All authors participated in discussions of the results and the preparation of the manuscript.

Competing interests
The authors declare no competing interests.

Additional information
Correspondence and requests for materials should be addressed to M.E. or Y.K.

Reprints and permission information is available at http://www.nature.com/reprints

Publisher's note Springer Nature remains neutral with regard to jurisdictional claims in published maps and institutional affiliations.